Heat transfer enhancement of ferrofluid flow in a solar absorber tube under non-uniform magnetic field created by a periodic current-carrying wire

A.Dahmani[a,*], J.Muñoz-Cámara[b], S.Laouedj[a], J.P. Solano[b]

[a] *Laboratory of Materials and Reactive Systems (LMSR), University Djillali Liabes of Sidi Bel Abbes, Algeria*
[b] *Dep. Ingeniería Térmica y de Fluidos, Universidad Politécnica de Cartagena Campus Muralla del Mar (30202) Cartagena, Spain*

doi: https://doi.org/10.1016/j.seta.2022.101996

Abstract

A novel configuration for heat transfer enhancement in parabolic trough solar collector absorbers by the use of a ferrofluid and an external magnetic field generated by a current-carrying wire is analyzed using numerical simulation. This new configuration consists of a wire which varies its position periodically along the tube. The analysis is focused on the study of the thermal hydraulic characteristics, Nusselt number and friction factor, and the average flow patterns in the turbulent flow regime ($15 \cdot 10^3 \leqslant Re \leqslant 250 \cdot 10^3$). In addition, different parameters of the periodic wire are analyzed: wire pitch and position angle. Ferrofluid Fe_3O_4 /Therminol 66 is considered for this application. Firstly, the effect of an increase on the magnetic field intensity is studied. The periodic wire configuration shows a higher increment of the Nusselt number in comparison to the straight wire for the same magnetic field increase. The results reveal that the presence of a non-uniform mag-

*Corresponding author
Email address: `da.abderraouf@gmail.com` (A.Dahmani)

Preprint submitted to Sustainable Energy Technologies and Assessments January 6, 2022

netic field generates a disturbed flow with a high velocity region near the current-carrying wire. The periodic wire configuration leads to a spatially-periodic behavior that increases the average Nusselt number and the friction factor, in comparison to a straight wire. Among the studied cases, the position angle $\theta = 30°$ and the pitch length $l = 3D$ are found to provide the maximum Nusselt number(Nu=244.25 for Re=15000).
Keywords: Parabolic trough solar collector, Ferrofluid, Magnetic field, FHD, Turbulent flow, CFD

Nomenclature

c_p	specific heat (J/(kg·K))
C_R	collector concentration ratio
D	absorber tube inner diameter (m)
D_e	absorber tube outer diameter (m)
d_p	particle diameter (m)
T	temperature (K)
H	magnetic field intensity vector modulus (A/m)
H_x	magnetic field intensity component in x direction (A/m)
H_y	magnetic field intensity component in y direction (A/m)
H_r	characteristic magnetic field intensity (A/m)
h	heat transfer coefficient (W/(m^2·K))
I	electric current (A)
I_g	global radiation (W/m^2)
I_b	beam radiation (W/m^2)
k	thermal conductivity (W/(m·K))

K_B	Boltzmann constant (=$1.3806503 \times 10^{-23} J/K$)
L	tube length (m)
l	wire pitch length (m)
M	magnetization (A/m)
m_p	particle magnetic moment(A.m^2)
P	pressure (Pa)
q''	heat flux (W/m^2)
V_{avg}	mean axial velocity (m/s)
x,y,z	directions
Dimensionless groups	
f	Darcy friction factor, $f = \frac{2\Delta P}{\rho_f V^2}(\frac{D}{L})$
Nu	Nusselt number, $Nu = \frac{hD}{k}$
Mn	Magnetic number, $Mn = \frac{\mu_0 \chi H_r^2 h^2}{\rho_f \nu_f^2}$
Pr	Prandtl number, $Pr = \frac{\mu c_p}{k}$
Re	Reynolds number, $Re = \frac{\rho V D}{\mu}$
Greek symbols	
α_f	thermal diffusivity (m^2/s)
φ	particle volume fraction
η_{th}	Thermal efficiency
ξ	Langevin parameter
μ	dynamic viscosity $(kg/(m \cdot s))$
μ_0	vacuum permeability (=$4\pi \times 10^{-7}$ $T \cdot m/A$)
μ_B	Bohr's magneton (=$9.27 \times 10^{-24} A \cdot m^2$)
ν	kinematic viscosity (m^2/s)
ρ	density (kg/m^3)

χ	magnetic susceptibility
Subscripts	
b	base fluid
f	ferrofluid
in	inlet
p	nanoparticle
w	wall
Abbreviations	
PTSC	parabolic trough solar collector
MF	magnetic field
HTF	heat transfer fluid

1. Introduction

Among the concentrated solar power (CSP) technologies, parabolic trough solar collectors represent a significant part of CSP's projects in the world [1, 2], as a promising alternative to conventional power generation plants. A parabolic trough solar collector (PTSC) mainly consists of a trough shape reflector that receives the direct solar irradiance and reflects it over a coated absorber tube, contained in an evacuated glass tube. The absorber tube contains the heat transfer fluid (HTF)[3], which depends on the application of the PTSC [4]. Compared to other clean energy harvest systems, the PTSC technology faces many engineering challenges to be competitive, so many studies have been carried out in order to enhance this technology's performance, e.g., by modifying the optical parameters of the PTSC [4, 5].

Many efforts are focused on increasing the tube side heat transfer rate in the absorber tube, and can be classified according to the traditional distinction between passive methods, like manipulating the geometrical characteristics of the device, and active methods, which require an additional energy supply [6]. Both types of techniques have been used by different research groups to enhance the performance in PTSCs.

Regarding passive methods, many works have proposed the use of inserts in the absorber tube [7, 8, 9] or the modification of the absorber tube shape [10, 11]. Moreover, many studies used nanoparticles to enhance the convective heat transfer of the HTF [12, 13, 14] by improving its thermal properties (thermal conductivity, mainly). On the other hand, other works have employed active methods, as rotating absorber tubes[15, 16].

During the last decade, the use of ferrofluids as HTF has attracted the interest of the heat transfer enhancement community: their magnetic properties give the ability to control heat transfer using external magnetic forces [17, 18], so, it can be considered as a compound technique. A ferrofluid is defined as the mixture of nano sized magnetic particles dispersed in a base fluid [19].

Since its development, the use of ferrofluids in presence of a magnetic field found many applications to enhance heat transfer, e.g., heat exchangers [20, 21], mini heat exchangers[22], flat plate solar collectors [23] and latent heat storage systems [24]. However, few studies studied the effect of magnetic fields on ferrofluids as HTF in PTSCs.

Shakiba and Vahedi [20] studied the pressure drop and heat transfer coefficient in a double pipe heat exchanger, where the inner tube contains a ferrofluid and an external non-uniform magnetic field is applied (generated by a current-carrying wire parallel to the tube). The authors observed that the magnetic field generated a Kelvin force, perpendicular to the ferrofluid flow, and a couple of vortices appeared as a consequence. This induced secondary flow lead to an increase of the Nusselt number of a 45% (for a $Re = 50$) in comparison to the case without magnetic field. The study also showed that the effect of the external magnetic field is reduced when the Reynolds number is increased.

One of the first studies to conceive the application of ferrofluids and an external magnetic field in parabolic trough solar collectors was performed by Khosravi et al. [25]. Their numerical study was focused on the turbulent region ($15 \cdot 10^3 < Re < 250 \cdot 10^3$). The different operating conditions were specified to those expected in the studied application: Therminol 66 was selected as HTF and the collector tube received a non-uniform heat flux. The results showed a significant increase on the Nusselt number and the friction factor when the magnetic field was applied. The authors concluded that the best performance was obtained when a 4 vol% Fe_3O_4-Therminol 66 mixture was used under the maximum magnetic field tested (500 G). Malekan et al. [26] extended the previous study to include different nanoparticles (CuO), nanoparticle size and the use of internal fins. The authors found that the Fe_3O_4 particles of the smallest size (10 nm) provided a higher heat transfer enhancement. Under external magnetic field, the introduction of the internal fins provided a modest increase on the performance evaluation criterion and a similar levelized cost of energy when compared to a smooth tube.

Soltanipour et al. [27] developed a numerical model to study the effect of an external magnetic field over a curved tube. This work was the first one to cover the influence of the current-carrying wire angular position on the flow characteristics. The results showed that the flow patterns (number of vortices and position) was strongly influenced by the wire position. The authors found that the optimal wire position corresponds to $\varphi = 180°$ (measured as the counter-clockwise angle with the horizontal axis), where the Kelvin force promotes the secondary flow recirculations produced by the tube curvature. The maximum heat transfer enhancement measured was about 29%. Yousefi et al. [28] investigated numerically the effect of the number of current-carrying wires and their positions on the hydro-thermal performance of ferrofluid flow in a flattened tube. Their results showed that the position and number of magnetic sources affects the flow pattern and the presence of two parallel wires lead to an important increase of convective heat transfer but also a higher pressure drop.

Based on the previous review, it is clear that ferrofluids under magnetic field effects as a compound heat transfer enhancement technique provide promising results for concentrated solar power applications. However, as it can be observed that these studies considered only an axially uniform magnetic field along the tube generated by a straight current-carrying wire, while other wire configurations have not been considered. This option appears as a reasonable solution for a higher heat transfer enhancement without a significant cost increase.

The present work focuses on the numerical study of a new current-carrying wire configuration for its application on PTSC absorbers. The proposed configuration is based on a periodic change of the wire position, introducing a periodic flow disturbance due to the variation of the magnetic field intensity along the tube. The proposed geometry introduces new geometrical parameters to be optimized: pitch length and angle position of the wire. A wide range of Reynolds numbers, $15 \cdot 10^3 < Re < 250 \cdot 10^3$, and Magnetic numbers, $1.52 \cdot 10^7 < Mn < 1.84 \cdot 10^9$, is analysed to quantify the effect of the new geometry on the heat transfer rate and pressure drop in the PTSC absorber.

2. Methodology

2.1. Problem description and theoretical formulation

Fig. 1a shows the three dimensional model of the studied parabolic trough solar collector (PTSC) absorber tube, equipped with a current-carrying wire, whose position varies periodically. In addition, the lower parts of the current-carrying wire are supposed to be attached to the glass tube keeping the wire fixed, while the two ends of the wire are connected to electricity source to generate the magnetic field. Figs. 1b-e depict the simplified model of the PTSC absorber tube, for the straight wire case (b and c) and the periodic wire (d and e). The tube is characterized by its inner and outer diameters, D and D_e, respectively, and the total length L. The ratio between the two diameters is D_e/D=1.06. The wire configuration is determined by the pitch length, l, the distance between the wire/s and the tube inner wall, R, and the angle θ, which measures the angle created by the y axis and the line connecting the wire and tube centers (Fig. 1d-e).

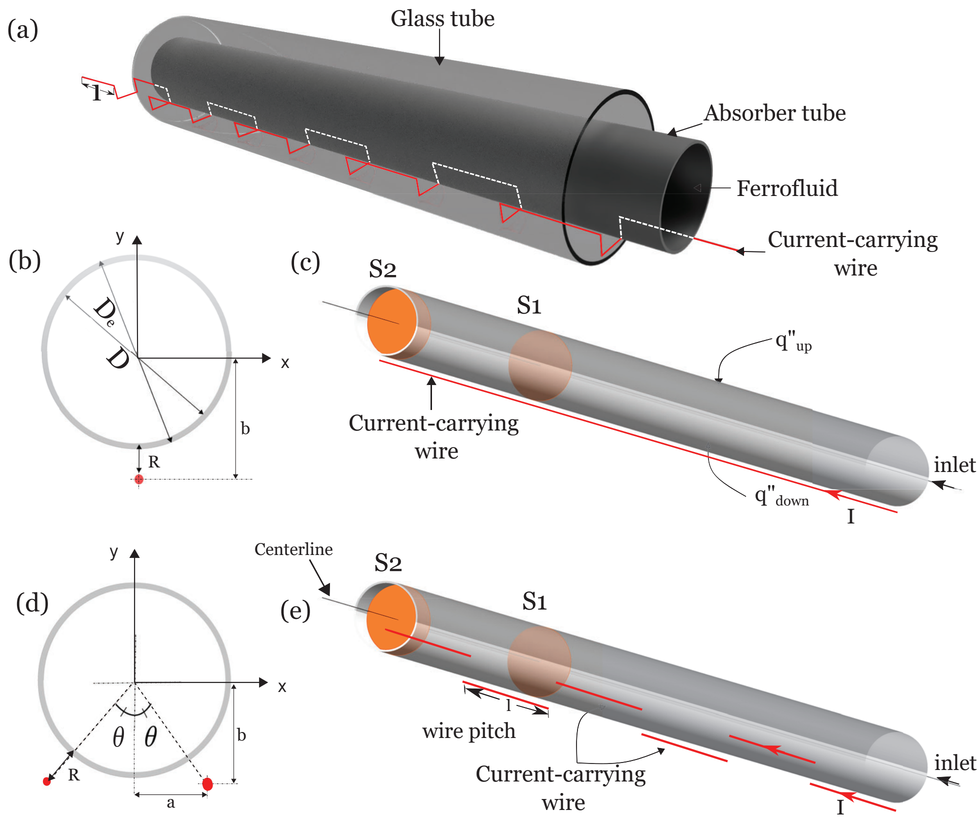

Fig. 1. a) 3D model for PTSC absorber tube, b) cross-sectional and c) 3D view of the straight wire case, d) cross-sectional and e) 3D view of the periodic wire case.

For the periodic wire configuration, only the magnetic field generated by the wire sections which are parallel to the tube axis is taken into account. The magnetic field generated by the connections between consecutive wire pitches has been neglected. A direct current, with intensity I, flows trough the wire in the positive z-axis direction. This current generates a magnetic field, $\vec{H}$, with two components, H_x and H_y, in the x and y directions, respectively. The values of the magnetic field components are given by Eqs. (1) and

(2)[29], and the representation of the vector and modulus of the magnetic field intensity is shown in Fig. 2a and Fig. 2b, respectively.

$$H_x(x, y) = \frac{I}{2\pi} \frac{(b - y)}{(x - a)^2 + (y - b)^2} \tag{1}$$

$$H_y(x, y) = \frac{I}{2\pi} \frac{(x - a)}{(x - a)^2 + (y - b)^2} \tag{2}$$

where a and b are the x and y coordinates of the wire, respectively, taking a coordinate system centered on the tube axis.

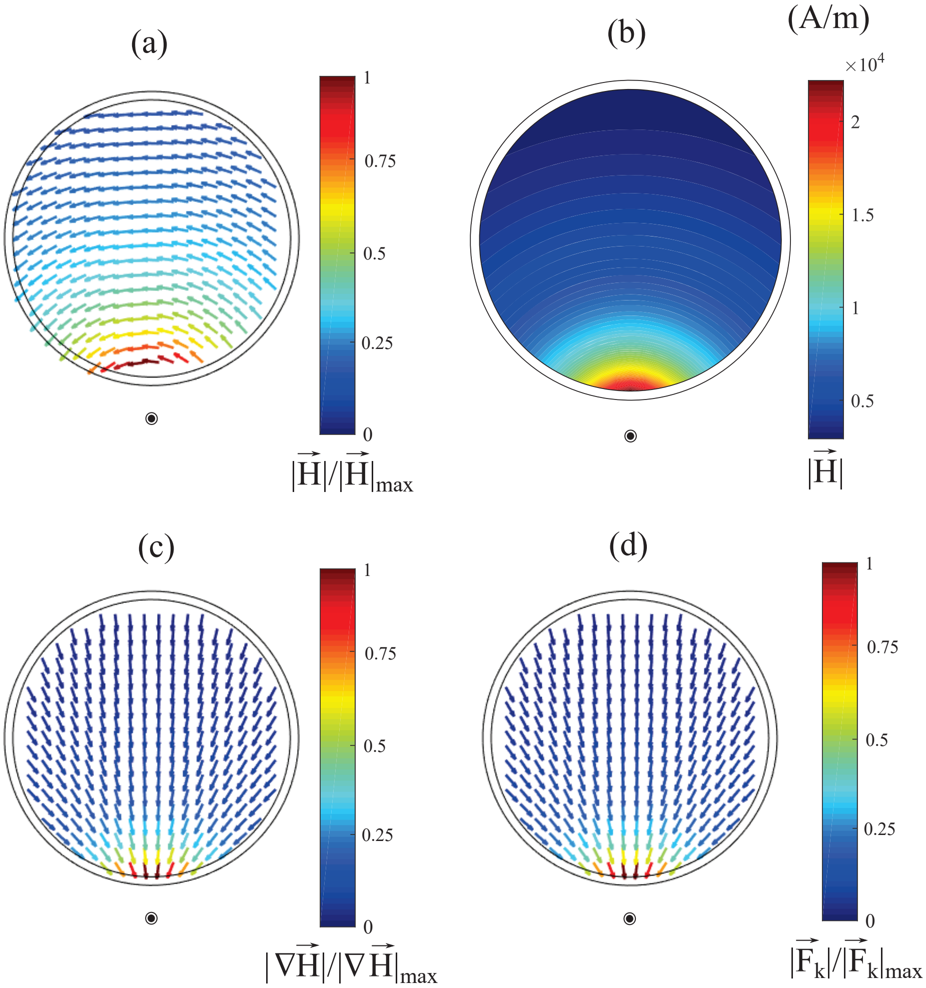

Fig. 2. Field calculations in a tube cross section for the Kelvin body force model: a) Vector field of the magnetic field intensity, b) Modulus of the magnetic field intensity, c) Gradient of the magnetic field, d) Kelvin body forces.

The heat transfer fluid (HTF) is the ferrofluid Fe_3O_4/Therminol 66, with a volume fraction φ=4% and a nanoparticle diameter d_p=10 nm. The fluid enters the tube with uniform velocity, V_{avg}, and temperature T_{in}. In addition, the heat flux applied on the tube is assumed to be non-uniform.

For this numerical investigation, single phase model is adopted for the steady turbulent flow of the ferrofluid, assuming that Fe_3O_4 nanoparticles and the base fluid (Therminol 66) are in thermal equilibrium and the slip velocity between them is negligible. The ferrofluid is also assumed to be incompressible, homogeneous and Newtonian (the thermo-physical properties of the base fluid and the nanoparticles are given in Table 1).

The interaction between the ferrofluid and the magnetic field generates the so-called Kelvin body force ($\vec{F_k}$), which is mathematically represented by Eq. (3).

$$\vec{F_k} = \mu_0(\vec{M} \cdot \nabla)\vec{H} \tag{3}$$

By applying the previous assumptions and considering that the magneto-caloric effect and the magnetohydrodynamic (MHD) term are negligible [27], the Kelvin body force (Eq. (3)) is the only term that arises in the momentum equation of the flow. In the absence of external magnetic field, this term would be zero. The components of the Kelvin body force are proportional to the gradient of the magnetic field intensity (Fig 2c), as given in Eqs. (4) and (5). They are represented in Fig 2d for a cross section of the tube. These terms are added to the right hand side of the momentum equations in the x and y directions, respectively [20, 27, 25, 30].

$$F_k(x) = \mu_0 M \frac{\partial H}{\partial x} \tag{4}$$

$$F_k(y) = \mu_0 M \frac{\partial H}{\partial y} \tag{5}$$

where M represents the magnetization and it is given by [24, 30]:

$$M = \frac{6\varphi m_p}{\pi d_p^3}(coth(\xi) - \frac{1}{\xi}) \tag{6}$$

where m_p represents the magnetic momentum and ξ is the Langevin parameter (see Eqs. (7) and (8)).

$$m_p = \frac{4\mu_B \pi d_p^3}{6 \times 91.25 \times 10^{-30}} \tag{7}$$

$$\xi = \frac{\mu_0 m_p H}{k_B T} \tag{8}$$

where μ_0,μ_B and K_B are the vacuum permeability, Bohr's magneton and Boltzmann constant, respectively.

In addition, the heat flux is applied at the tube outer wall, taking in consideration the simplified local concentration ratio (LCR) model [26, 31]. This model assumes that the tube receives a uniform heat flux on its upper half, equals to the global radiation I_g (Eq. (9)), while the lower half is exposed to a uniform heat flux $q"_{down}$, equals to the concentrated radiation beams reflected by the PTSC (Eq. (10)). For the current study: $I_g = 680\ W/m^2$, $I_b = 630\ W/m^2$, and the concentration ratio is $C_R = 15.46$.

$$q"_{up} = I_g \tag{9}$$

$$q"_{down} = I_b C_R \tag{10}$$

2.2. *Thermo-physical properties*

The ferrofluid density, specific heat, dynamic viscosity and thermal conductivity are calculated using the thermo-physical properties in Table 1 and the following correlations [26]:

Table 1: The thermo-physical properties of base fluid, nanoparticles and the ferrofluid [26].

Material	$\rho(kg/m^3)$	$c_p(J/kgK)$	$k(W/mK)$	$\mu(kg/ms)$
Therminol 66	899.5	2122	0.107	0.00106
Fe_3O_4	5200	670	6	-
Ferrofluid ($\varphi = 4\%$)	1071.5	2063.92	0.119657	0.001166

$$\rho_f = \varphi\rho_p + (1-\varphi)\rho_b \tag{11}$$

$$c_{p,f} = \varphi c_{p,p} + (1-\varphi)c_{p,b} \tag{12}$$

$$\mu_f = (1+2.5\varphi)\mu_b \tag{13}$$

$$k_f = \left[\frac{k_p + (n-1)k_b - (n-1)\varphi(k_b - k_p)}{k_p + (n-1)k_b - \varphi(k_b - k_p)}\right] k_b \tag{14}$$

where n refers to the empirical shape factor of the nanoparticles, which is n=3 for the studied case (spherical particles) [20, 32].

2.3. Numerical procedure and boundary conditions

Finite volume method is used to solve the governing equations numerically by means of the commercial CFD code ANSYS® Fluent release 17.1 [33], using a SIMPLEC algorithm running in parallel mode. The turbulence has been modelled with the $k-\epsilon$ RNG model, which has been selected based on previous literature [25, 31]. Moreover, the Kelvin body force components are added as source terms to the momentum equations in x and y directions (Eqs. (8) and (9), respectively) by implementing a user defined function (UDF). A value for the residuals lower than 10^{-5} for the continuity and momentum equations and 10^{-9} for the energy equation is considered as convergence criterion.

As boundary conditions, the ferrofluid enters the PTSC absorber tube with a uniform velocity $V = V_{avg}$ and an inlet temperature of $T_{in} = 230°C$. The inlet velocity is calculated in order to obtain the desired Reynolds number in the studied range, $15000 \leqslant Re \leqslant 250000$. The pressure at the tube outlet is assumed to be zero.

2.4. Data reduction

Darcy's friction factor has been computed using its common definition:

$$f = \frac{2\Delta P}{\rho_f V^2}\left(\frac{D}{L}\right) \tag{15}$$

where the pressure drop, ΔP, has been calculated as the difference between the area-weighted average static pressure at sections S1 and S2 (depicted in Fig. 1), where the flow is hydrodynamically and thermally fully developed. The length L is the distance between sections S1 and S2.

The calculation of the average Nusselt number has to take into account the axial variation of the heat transfer coefficient, which varies along each wire pitch due to the periodic perturbation produced by the different wire positions.

The peripherally averaged convection coefficient, at each axial position, is obtained as:

$$\bar{h}(x) = \frac{q''}{\bar{T}_{iw}(x) - T_b(x)} \tag{16}$$

where $\bar{T}_{iw}(x)$ is the peripherally averaged inner wall temperature at the axial position x:

$$\bar{T}_{iw}(x) = \frac{\sum_{i=1}^{n_{nodes}} T_i(x)}{n_{nodes}}; \forall i : r_i = D/2 \tag{17}$$

and $T_b(x)$ is the bulk temperature [34] at the axial location x:

$$T_b(x) = \frac{\sum_{i=1}^{n_{cells}} \rho_i c_{pi} T_i(x) u_i(x) A_i}{\dot{m}\ c_p} \tag{18}$$

The local convection coefficient is averaged along the distance between sections S1 and S2 (Fig. 1). Finally, the average Nusselt number is derived:

$$Nu = \frac{h_{avg} D}{k} \tag{19}$$

The Reynolds number and the Prandtl number have been calculated according to their common definitions. In addition, another dimensionless number must be introduced in order to account for the effect of the magnetic field intensity on the flow behaviour. The definition of the Magnetic number, used by Soltanipour et al. [27], has been considered:

$$Mn = \frac{\mu_0 \chi H_r^2 D^2}{\rho_f \nu_f^2} \tag{20}$$

where H_r is the characteristic magnetic field, which in this work corresponds to the magnetic field measured at the tube inner wall point which is closer to the current-carrying wire:

$$H_r = \frac{I}{2\pi R} \tag{21}$$

This value is constant along the axial direction, in spite of the variation of the wire position, because the distance between the current carrying wire and the absorber tube inner wall, R, is kept constant (see Fig. 1).

2.5. Mesh sensitivity analysis and validation

In order to ensure that the selected mesh provides accurate results and requires a reasonable computational time, a sensitivity study was performed. The friction factor was chosen as a relevant quantity to compare the accuracy of the different mesh sizes. Three different meshes, ranging from 1.87 to 5.69 million elements, were tested, at two Reynolds numbers, $Re = 15000$ and $Re = 250000$, covering the range tested in this work. The results are summarized in Table 2, where the deviation of the calculated friction factor is compared (as a percentage) to that provided by the finest mesh.

As can be observed, the coarsest mesh provides good results at the lowest Reynolds number, but the deviation becomes unacceptable at the highest Reynolds number, around 8%. On the other hand, the intermediate mesh shows a very low deviation even at the highest Reynolds number, 0.1%, value that has been considered as accurate enough. The selected mesh is shown in

Table 2: Friction factor comparison for the three studied meshes at Re=15000 and Re=250000.

Number of elements	$Re = 15 \cdot 10^3$	$Re = 250 \cdot 10^3$
1.87·10^6	0.2%	7.8%
3.71·10^6	0.03%	0.10%
5.69·10^6	(f=0.0299)	(f=0.0147)

Fig. 3, where the mesh refinement in the zone adjacent to the wall (where the higher velocity gradients are expected) can be seen in detail.

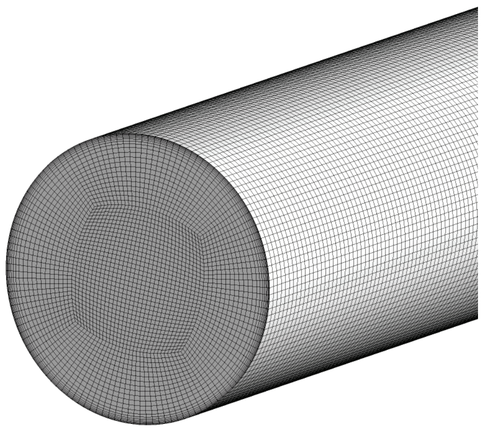

Fig. 3. The studied model mesh.

The numerical methodology has been validated by comparison of the variables of interest with well-known correlations in the range tested. Blasius' equation [35], Petukhov's correlation [36] and Gnielinski [37] have been considered for the friction factor and the Nusselt number, respectively.

Darcy's friction factor is plotted in Fig. 4a as a function of the Reynolds number, in the absence of magnetic field. As expected, the simulations with pure Therminol 66 and Therminol 66 with nanoparticles clearly overlap. The maximum deviation of the simulations is around 5%, which can be considered as accurate enough for validation purposes. In Fig. 4b, the average Nusselt number is shown as a function of the Reynolds number and compared with the correlation for fully turbulent flow proposed by Gnielinski [37]. The results are in good agreement with the correlation, with a deviation lower than a 18% in the whole range.

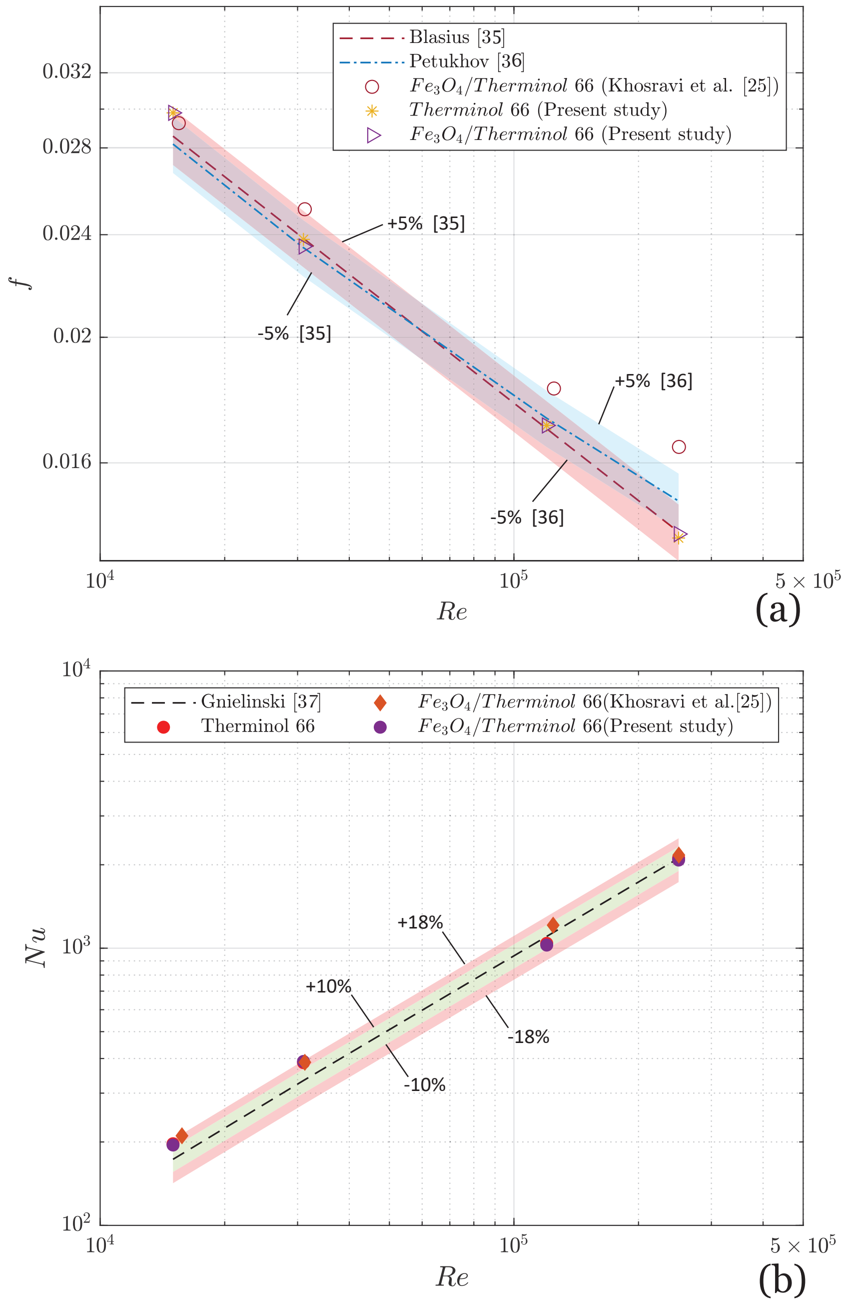

Fig. 4. a) Comparison of the obtained friction factor values with previous studies, b) comparison of the average Nusselt number values with Gnielinski's correlation [37].

3. Results and discussion

3.1. Effect of the magnetic number

The effect of the magnetic field intensity on the average Nusselt number is analyzed in Fig. 5a, at a Reynolds number $Re = 15000$, for the two wire configurations (straight or periodic). On the right axis, the increase in the Nusselt number in comparison to the reference case (without magnetic field applied) is also indicated. According to the results, increasing the Magnetic number from Mn=1.52×10^7 to Mn=1.84×10^9 leads to an increment on the Nusselt number for both configurations. However, the increment for the straight wire configuration is more subtle if it is compared with the periodic configuration, with an increase of around 5% and 25%, respectively.
The effect of the Magnetic number, from Mn=$1.52 \cdot 10^7$ to Mn=$1.84 \cdot 10^9$, on the friction factor is illustrated in Fig. 5b. The right axis represents the friction factor increase, as a percentage, comparing to the reference value with no applied magnetic field ($Mn = 0$). For both configurations with Mn=1.52×10^7 , there is no significant increase in the friction factor, around a 2 %, but an increase in the Magnetic number increases the friction factor around 7 % for the straight wire case, in contrast to the periodic wire, which shows an increment of around 9 %. Thus, it must be highlighted the close relation between the heat transfer and the pressure drop results, a Nusselt number increase implies an increase in the friction factor.

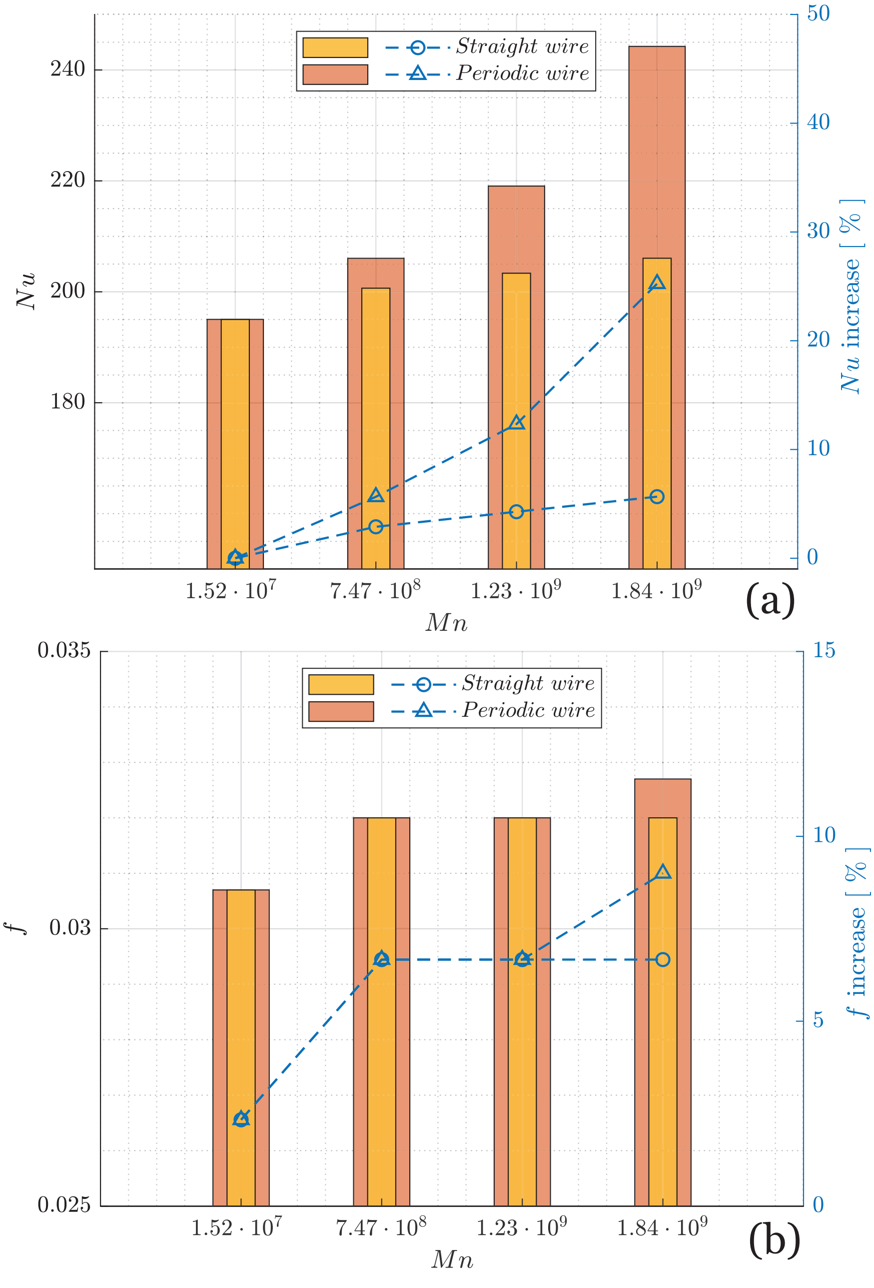

Fig. 5. Effect of different wire configurations and the Magnetic number on a) the Nusselt number b) friction factor, at Re=15000.

3.2. Effect of current-carrying wire configuration

The 3D dimensionless axial velocity profiles of Fe_3O_4/Therminol 66 ferrofluid flow are depicted in Figs. 6(a-c) at the axial position z=22.7$\cdot D$ and Re=15000. Fig. 6a shows an axisymmetric profile for the case in absence of external magnetic forces, whereas Figs. 6(b,c) show the deformation of the axial velocity profile in presence of the Kelvin body force due to the magnetic field, as it was observed in previous studies [38, 20]. In the case of the straight current-carrying wire Fig. 6b, it is noticeable a high velocity region near the current-carrying wire, while the periodic wire case (Fig. 6c) shows an asymmetric pattern with two velocity peaks. The current wire at the current wire position generates a peak (similarly to the straight wire), while the other weaker peak can be justified by the flow inertia: the flow is still evolving from the previous pitch, where the wire was placed at the opposite position.

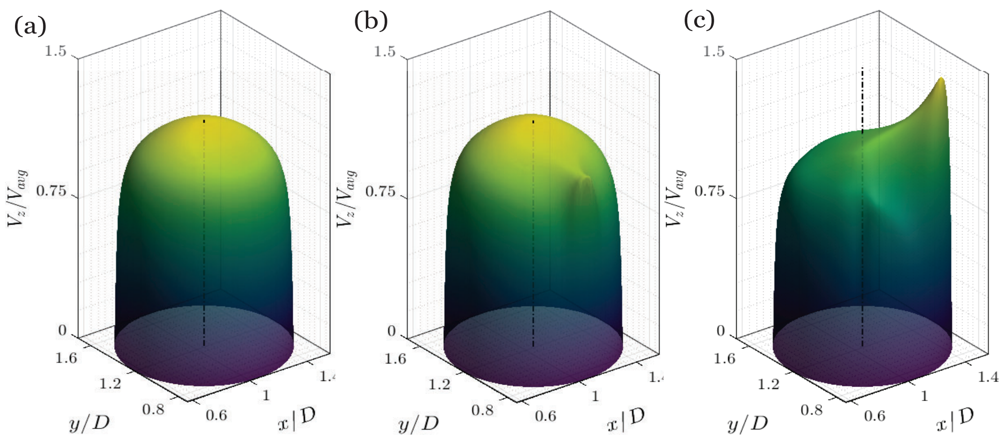

Fig. 6. Dimensionless axial velocity 3D profiles of ferrofluid flow at the axial position z=22.7·D, for Re 15000 a) Mn=0, b) Straight current-carrying wire case, Mn=$1.84 \cdot 10^9$ c) periodic current-carrying wire case, Mn=$1.84 \cdot 10^9$, pitch length: $l/D = 3$ and $\theta = 30°$.

Furthermore, Fig. 7 shows the longitudinal behavior of the axial velocity at the tube center axis along the z direction for different configurations. Obviously, the axial velocity (which enters the tube with a uniform profile) develops until it reaches a maximum constant value at the fully developed region. The straight wire shows a similar behaviour to the case with $Mn = 0$, the flow develops and the tube center is far from the current-carrying wire, so little effect is found on the axial velocity. On the contrary, the periodic wire displays a spatially-periodic pattern, there is an initial developing region but after 4-5 pitches the flow reaches periodicity. This can be explained by the periodicity of the external magnetic field which is perceived by the flow. In addition, it is a noticeable that the length of the repeated pattern matches the simulated pitch length, $l = 6D$.

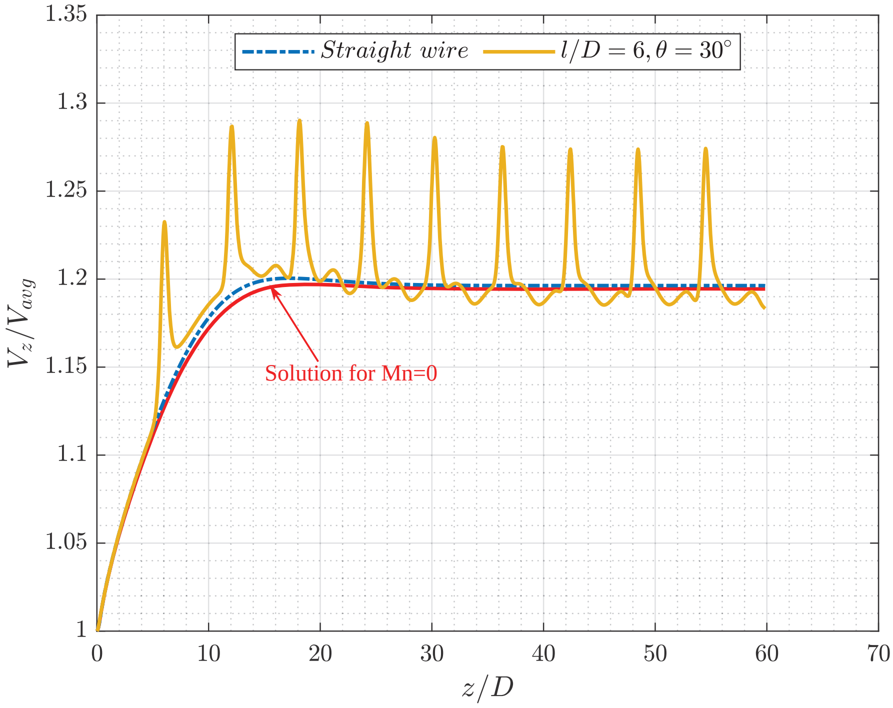

Fig. 7. Dimensionless axial velocity at the tube center along the z direction for both wire configurations, Re=15000 and Mn=$1.84 \cdot 10^9$.

The dimensionless axial velocity contours in Fig. 8 reveal the distribution of the velocity at Re=15000 in three different cross sections located at z=16.7D, z=19.7·D and z=22.7·D for a Magnetic number Mn=0 (Fig. 8a), Mn=$1.84 \cdot 10^9$ generated by the straight wire (Fig. 8b) and the periodic wire (case of pitch length l=3·D, and position angle $\theta = 30°$) (Fig. 8c). For the straight wire case (Fig. 8b), it can be noticed that the magnetic field increases the high velocity towards the wire position at the bottom part of the tube. On the contrary, the axial velocity distribution in the case of the periodic wire shows that the high velocity region changes its position along the tube (a pitch at the right and the next pitch at the left). This also explains the oscillating behavior of the axial velocity curves along the axial direction in Fig. 7 for the periodic current-currying wires cases.

There is an apparent mismatch between the wire position and the high velocity region, that can be explained by the flow inertia. The initial wire accelerates the fluid close to this but, once it reaches a high velocity, the wire position is changed so the high velocity region, close to the initial wire position, is still observed in the following pitch. This process is repeated along the tube generating a lag between the action (magnetic force) and the flow reaction (high velocity region).

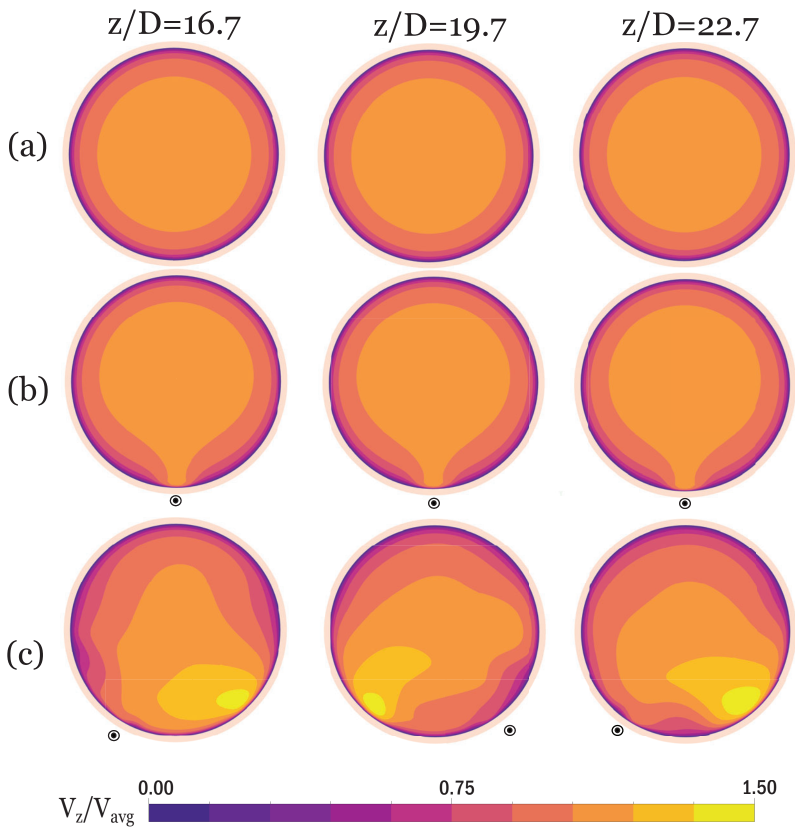

Fig. 8. Dimensionless axial velocity (V_z/V_{avg}) contours for Re=15000. a) Mn=0, b) Straight wire case, Mn=$1.84 \cdot 10^9$ c) periodic wire case, Mn=$1.84 \cdot 10^9$, pitch length $l/D = 3$ and $\theta = 30°$.

For the sake of a deeper understanding of the non-uniform magnetic field effect on the ferrofluid flow pattern, streamlines on the cross section (of the average velocity field) are plotted in Fig. 9. They have been colored according to the local dimensionless axial velocity, V_z/V_{avg}. The transversal streamlines (Fig. 9) reveals the creation of a pair of counter-rotating vortices for both cases, straight (a) and periodic wires (b). The vortices size in the fully developed region is uniform along the axial direction for the straight wire case (a). However, for the periodic wire case (b), the vortex size depends on the axial position, eventually the wire pitch position. The increase and decrease of the vortices size varies periodically, like the high axial velocity zone, along the axial direction.

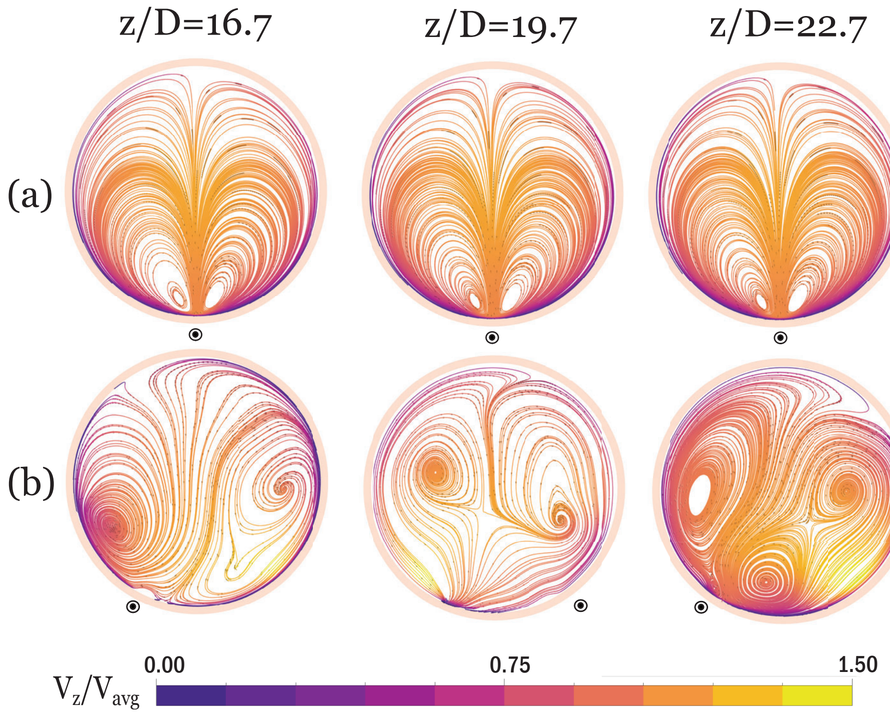

Fig. 9. Effect of magnetic field on surface streamlines of ferrofluid flow in PTSC absorber tube at different cross-sections, for Re=15000 a) Mn=0, b) Straight current-carrying wire case, Mn=$1.84 \cdot 10^9$ c) periodic wire case, Mn=$1.84 \cdot 10^9$, pitch length $l/D = 3$ and $\theta = 30°$.

In order to analyze the effect of the magnetic field on the convective heat transfer, the average Nusselt number, Nu, is plotted as a function of the Reynolds number, Re, in Fig. 10a. The data for Therminol 66 and Fe_3O_4/Therminol 66 as working fluids under non uniform heat flux are included, with and without applied magnetic field, and for different current-carrying wire configurations.

The application of a magnetic field, Mn=$1.84 \cdot 10^9$, increases the Nusselt number in the range of Reynolds numbers from Re=15000 to Re=120000. The periodic configuration increases the Nusselt number comparing to the straight wire case for the same Magnetic number.

Fig. 10b shows Darcy's friction factor as a function of the Reynolds number. The application of a magnetic field increases the friction factor for both wire configurations, and higher friction factor values are observed for the periodic configuration in comparison to the straight wire configuration. Moreover, the relative pitch length of the wire (l/D) has a noticeable effect on the friction factor value for the studied Magnetic number, Mn=$1.84 \cdot 10^9$, with higher values for the lower pitch, $l = 3D$.

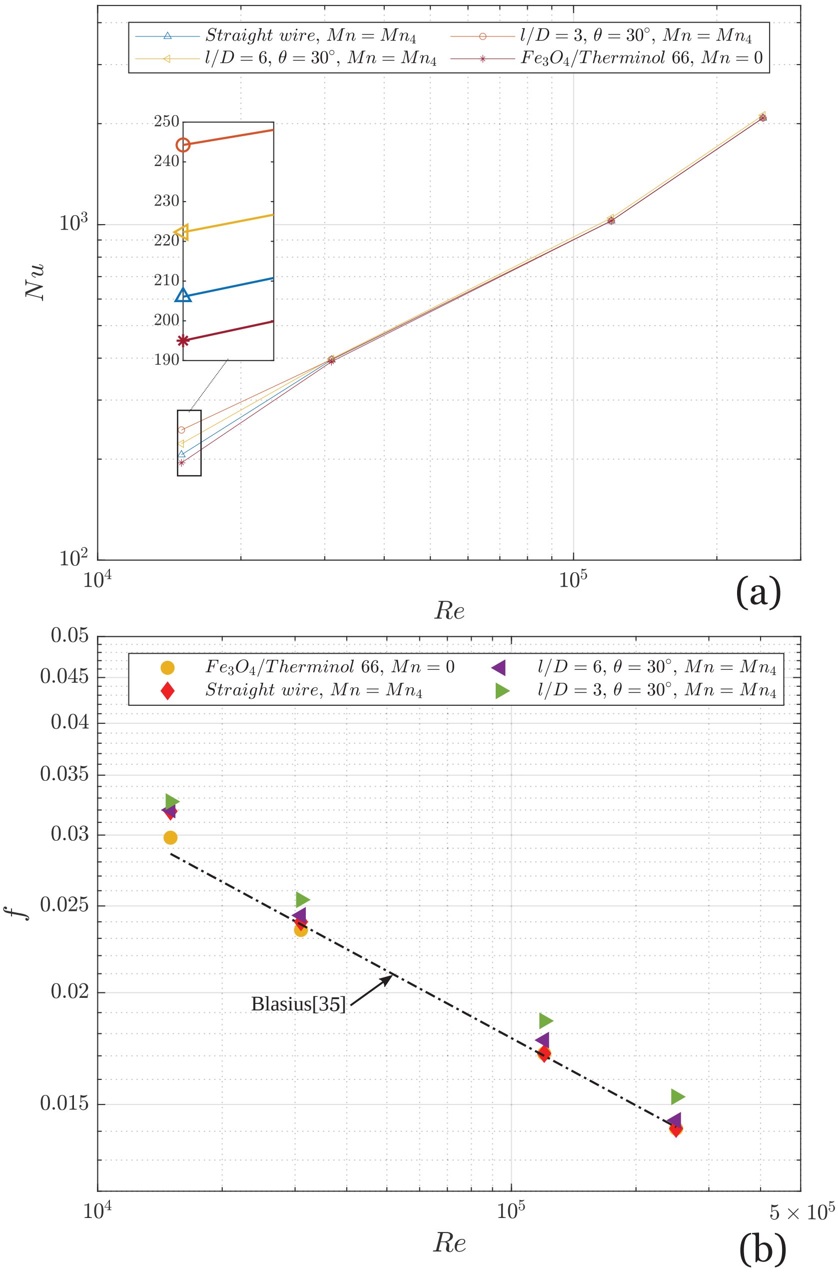

Fig. 10. Effect of the magnetic field (Mn=$1.84 \cdot 10^9$) generated by straight and periodic wires on a) the Nusselt number b) Darcy's friction factor, as functions of the Reynolds number.

3.3. Effect of periodic current-carrying wire pitch position

In order to see the effect of the wire location for the periodic configuration cases, the Nusselt number as a function of the Reynolds number is plotted in Fig. 11a for various half-angles: $\theta = 15°$, $\theta = 30°$ and $\theta = 90°$; while the other relevant parameters are kept constant: Magnetic number (Mn=$1.84 \cdot 10^9$), pitch length (l=$3{\cdot}D$) and wire-tube center distance. Clearly, putting the wire pitches at an intermediate angle, $\theta = 30°$, leads to an increase on the Nusselt number.

Fig. 11b represents the effect of the half-angle between consecutive wire pitches on the friction factor. The results for all the half-angles tested are significantly higher than the straight wire configuration, as expected from the previous Nusselt number results. However, the variation of the friction factor for the different pitches is almost unnoticeable. Thus, it simplifies the selection of the optimum half-angle, the case of $\theta = 30°$ increases the heat transfer but does not imply a significant pressure drop increase.

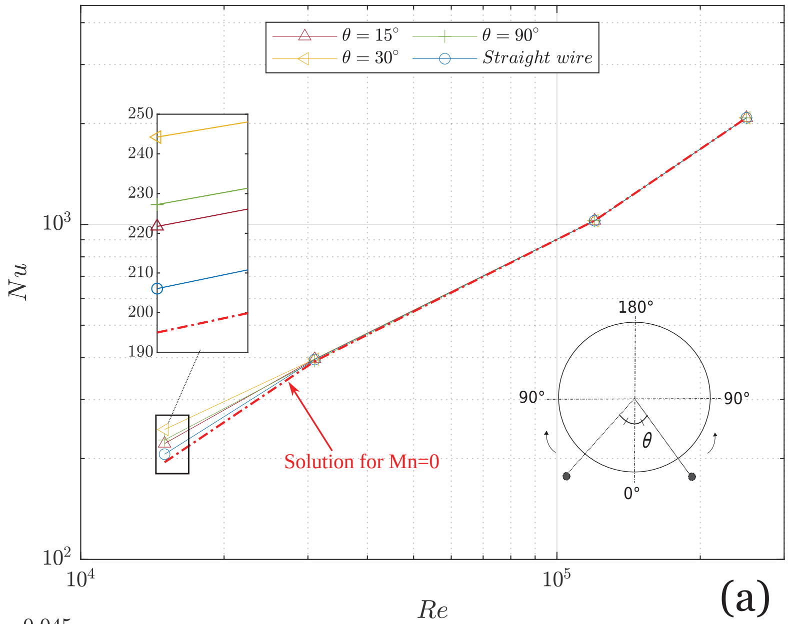

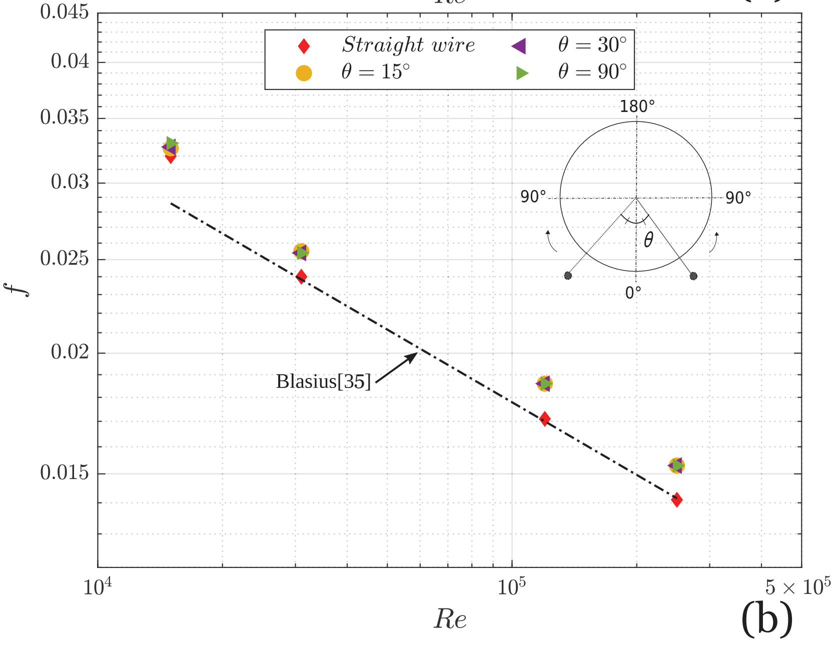

Fig. 11. The effect of the wire pitch position on a) the Nusselt number b) friction factor. Mn=$1.84 \cdot 10^9$, $l/D = 3$.

3.4. Thermal efficiency

Since the thermal efficiency is a fundamental parameter for the characterization of PTSC, Fig. 12 shows the thermal efficiency (η_{th}) for three different working conditions as a function of Reynolds number. The thermal efficiency is calculated using Eq. (22)

$$\eta_{th} = \frac{q''}{q'' + q_{loss}} \tag{22}$$

where the heat losses (q_{loss}) has been calculated according to the model proposed by Mohamad et al. [39].

The results show that the thermal efficiency is higher at higher Reynolds numbers for all cases. However, the use of the ferrofluid enhances the thermal efficiency for Reynolds number Re=15000 in the presence of the magnetic field in comparison to the base fluid case, with an enhancement of 0.53 % and 1.35 % successively (see right axis Fig. 12). In contrast, the enhancement margin by the magnetic field tends to be negligible by the increase of the inertial forces.

On the other hand, a comparison between the obtained results using this compound technique (active and passive techniques) and the results from the literature shows the possibility to achieve similar or better enhancement margin using other nanofluids without the need for additional external power (see Table 3).

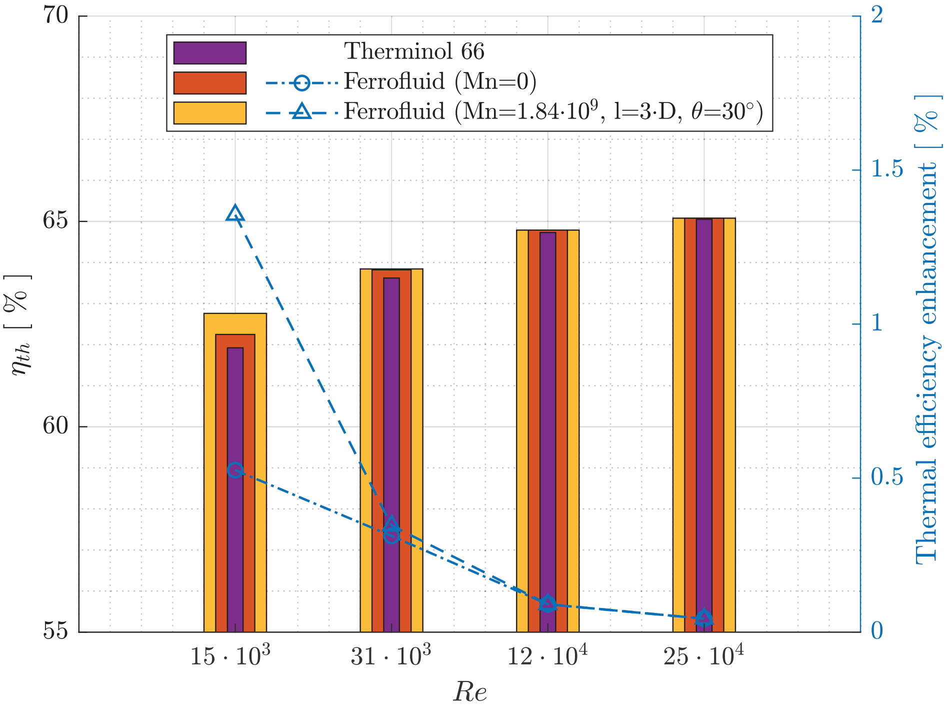

Fig. 12. The thermal efficiency and thermal efficiency enhancement.

Table 3: The thermal efficiency enhancement compared to other studies.

Case	enhancement (%)
Present study (Ferrofluid (Mn=$1.84 \cdot 10^9$, $l/D = 3$))	1.35 %
Syltherm 800 with Al_2O_3 and TiO_2 [40]	1.31 %
Therminol VP1 with SWCNT nano particles [41]	4.4 %

4. Conclusions

1. Flow of ferrofluid in parabolic trough solar collector absorber, integrated with a new current-carrying wire configuration, has been numerically analyzed. This study provides an insight on how the magnetic field affects the hydro-thermal characteristics of the ferrofluid flow.
2. The effect of a magnetic field generated by straight and periodic current-carrying wires on the 3D axial velocity profiles has been visualized. The MF generated by the straight wire creates a high velocity region near the wire position, while the periodic wire generates an asymmetric profile with spatially-periodic deformation along the PTSC absorber.
3. The spatial periodicity of velocity profile for the periodic wire configuration cases is due to the periodic disturbance of the flow produced by the change of direction of the Kelvin forces.
4. The increase of the Magnetic number yields an increase in the Nusselt number and the friction factor. The difference on the Nusselt number and friction factor between the straight wire and the periodic wire is also increased at higher Mn. The effect of the Mn decreases at higher Reynolds numbers due to the increase in the inertial forces.
5. The present study showed that an increase in the Nusselt number, but also in the friction factor, could be achieved for the same Magnetic number by changing the wire configuration.
6. The optimum configuration (under the studied conditions) was found for a position angle of $\theta = 30^\circ$ and a pitch length $l = 3D$.
7. The use of the magnetic field enhanced the thermal efficiency of the PTSC by up to 1.35 %.

8. The use of ferrofluid and a MF generated by electrical current-carrying wire is expensive at the studied Reynolds numbers range comparing to other models using passive methods. However, this technique could be promising at lower Reynolds number.

Acknowledgements

The first author gratefully acknowledges Universidad Politécnica de Cartagena for providing the high performance computing hardware. He is also grateful to M. Malekan and H. Khaboshan for their comments and advices.

References

[1] J. Fredriksson, M. Eickhoff, L. Giese, M. Herzog, A comparison and evaluation of innovative parabolic trough collector concepts for large-scale application, Solar Energy 215 (2021) 266–310.

[2] P. Forman, S. Penkert, C. Kämper, T. Stallmann, P. Mark, J. Schnell, A survey of solar concrete shell collectors for parabolic troughs, Renewable and Sustainable Energy Reviews 134 (2020) 110331.

[3] A. Raheem, W. Siddique, Z. H. Farooqui, T. Salameh, I. ul Haq, K. Waheed, K. Qureshi, Performance evaluation of adding helical-screw tape inserts in parabolic solar trough collectors as a source of cleaner energy production, Journal of Cleaner Production 297 (2021) 126628.

[4] G. Manikandan, S. Iniyan, R. Goic, Enhancing the optical and thermal efficiency of a parabolic trough collector – a review, Applied Energy 235 (2019) 1524–1540.

[5] M. C. Kulahli, S. Akbulut Özen, A. B. Etemoglu, Numerical simulation of a parabolic trough collector containing a novel parabolic reflector with varying focal length, Applied Thermal Engineering 161 (2019) 114210.

[6] T. Alam, M.-H. Kim, A comprehensive review on single phase heat transfer enhancement techniques in heat exchanger applications, Renewable and Sustainable Energy Reviews 81 (2018) 813–839.

[7] E. Bellos, I. Daniil, C. Tzivanidis, Multiple cylindrical inserts for parabolic trough solar collector, Applied Thermal Engineering 143 (2018) 80–89.

[8] E. Bellos, C. Tzivanidis, D. Tsimpoukis, Optimum number of internal fins in parabolic trough collectors, Applied Thermal Engineering 137 (2018) 669–677.

[9] B. Zou, Y. Jiang, Y. Yao, H. Yang, Thermal performance improvement using unilateral spiral ribbed absorber tube for parabolic trough solar collector, Solar Energy 183 (2019) 371–385.

[10] O. Chakraborty, B. Das, R. Gupta, S. Debbarma, Heat transfer enhancement analysis of parabolic trough collector with straight and helical absorber tube, Thermal Science and Engineering Progress 20 100718.

[11] M. Shafiey Dehaj, M. Rezaeian, D. Mousavi, S. Shamsi, M. Salarmofrad, Efficiency of the parabolic through solar collector using nife2o4/water nanofluid and u-tube, Journal of the Taiwan Institute of Chemical Engineers (2021).

[12] Y. Wang, J. Xu, Q. Liu, Y. Chen, H. Liu, Performance analysis of a parabolic trough solar collector using al2o3/synthetic oil nanofluid, Applied Thermal Engineering 107 (2016) 469–478.

[13] A. Benabderrahmane, M. Aminallah, S. Laouedj, A. Benazza, J. P. Solano, Heat Transfer Enhancement in a Parabolic Trough Solar Receiver using Longi- tudinal Fins and Nanofluids 25 (5) (2016) 410–417.

[14] J. Subramani, P. Nagarajan, O. Mahian, R. Sathyamurthy, Efficiency and heat transfer improvements in a parabolic trough solar collector using tio2 nanofluids under turbulent flow regime, Renewable Energy 119 (2018) 19–31.

[15] A. M. Norouzi, M. Siavashi, M. H. Khaliji Oskouei, Efficiency enhancement of the parabolic trough solar collector using the rotating absorber tube and nanoparticles, Renewable Energy 145 (2020) 569–584.

[16] M. Bezaatpour, H. Rostamzadeh, J. Bezaatpour, Hybridization of rotary absorber tube and magnetic field inducer with nanofluid for performance enhancement of parabolic trough solar collector, Journal of Cleaner Production 283 (2021) 124565.

[17] H. Yamaguchi, Engineering Fluid Mechanics, Vol. 85 of Fluid Mechanics and Its Applications, SPRINGER, 2008, p. 497.

[18] M. Alsaady, R. Fu, B. Li, R. Boukhanouf, Y. Yan, Thermo-physical properties and thermo-magnetic convection of ferrofluid, Applied Thermal Engineering 88 (2015) 14–21.

[19] R. Rosensweig, Ferrofluids: Introduction, in: Reference Module in Materials Science and Materials Engineering, Elsevier, 2016. doi:10.1016/B978-0-12-803581-8.02477-2.

[20] A. Shakiba, V. Khodadad, Numerical analysis of magnetic field effects on hydro-thermal behavior of a magnetic nanofluid in a double pipe heat exchanger, Journal of Magnetism and Magnetic Materials 402 (2016) 131–142.

[21] F. Fan, C. Qi, J. Tang, Q. Liu, X. Wang, Y. Yan, A novel thermal efficiency analysis on the thermo-hydraulic performance of nanofluids in an improved heat exchange system under adjustable magnetic field, Applied Thermal Engineering 179 (2020) 115688.

[22] M. Bezaatpour, M. Goharkhah, Convective heat transfer enhancement in a double pipe mini heat exchanger by magnetic field induced swirling flow, Applied Thermal Engineering 167 (2020) 114801.

[23] M. Bezaatpour, H. Rostamzadeh, Design and evaluation of flat plate solar collector equipped with nanofluid, rotary tube, and magnetic field inducer in a cold region, Renewable Energy 170 (2021) 574–586.

[24] E. Shi, S. Ahangar Zonouzi, H. Aminfar, M. Mohammadpourfard, Enhancement of the performance of a nepcm filled shell-and-multi tube thermal energy storage system using magnetic field: A numerical study, Applied Thermal Engineering 178 (2020) 115604.

[25] A. Khosravi, M. Malekan, M. E. H. Assad, Numerical analysis of magnetic field effects on the heat transfer enhancement in ferrofluids for a parabolic trough solar collector, Renewable Energy 134 (2019) 54–63.

[26] M. Malekan, A. Khosravi, S. Syri, Heat transfer modeling of a parabolic trough solar collector with working fluid of fe3o4 and cuo/therminol 66 nanofluids under magnetic field, Applied Thermal Engineering 163 (2019).

[27] H. Soltanipour, A. Gharegöz, M. B. Oskooee, Numerical study of magnetic field effect on the ferrofluid forced convection and entropy generation in a curved pipe, Journal of the Brazilian Society of Mechanical Sciences and Engineering 42 (3) (2020) 1–15.

[28] E. Yousefi, H. R. Nazif, H. Najafi Khaboshan, A. Azarinia, Non-Uniform Magnetic Field Effect on Forced Convection Heat Transfer of Flattened

Tubes Using Two-Phase Mixture Model, Heat Transfer Engineering 42 (12) (2021) 1041–1058.

[29] M. Hangi, M. Bahiraei, A. Rahbari, Forced convection of a temperature-sensitive ferrofluid in presence of magnetic field of electrical current-carrying wire : A two-phase approach, Advanced Powder Technology 29 (9) (2018) 2168–2175.

[30] S. M. Mousavi, M. Biglarian, A. A. R. Darzi, M. Farhadi, H. H. Afrouzi, D. Toghraie, Heat transfer enhancement of ferrofluid flow within a wavy channel by applying a non-uniform magnetic field, Journal of Thermal Analysis and Calorimetry 139 (5) (2020) 3331–3343.

[31] S. Ebrahim Ghasemi, A. Akbar Ranjbar, Numerical thermal study on effect of porous rings on performance of solar parabolic trough collector, Applied Thermal Engineering 118 (2017) 807–816.

[32] A. Farhad, Aamina, I. Khan, N. A. Sheikh, M. Gohar, I. Tlili, Effects of different shaped nanoparticles on the performance of engine-oil and kerosene-oil: A generalized brinkman-type fluid model with non-singular kernel, Scientific Reports 8 (1) (2018) 1–13.

[33] ANSYS® FLUENT, Release 17.1, User's Guide, ANSYS, Inc.

[34] Y. Çengel, A. Ghajar, Heat and Mass Transfer: Fundamentals & Applications, McGraw Hill Education, 2015.

[35] H. Blasius, Das aehnlichkeitsgesetz bei reibungsvorgängen in flüssigkeiten, in: Mitteilungen über Forschungsarbeiten auf dem

Gebiete des Ingenieurwesens: insbesondere aus den Laboratorien der technischen Hochschulen, Springer Berlin Heidelberg, Berlin, Heidelberg, 1913, pp. 1–41.

[36] B. Petukhov, Heat transfer and friction in turbulent pipe flow with variable physical properties, Vol. 6 of Advances in Heat Transfer, Elsevier, 1970, pp. 503–564.

[37] V. Gnielinski, New equations for heat and mass transfer in turbulent pipe and channel flow, International Chemical Engineering 16 (2) (1976) 359–368.

[38] H.Aminfar, M. Mohammadpourfard, S. Zonouzi, Numerical study of the ferrofluid flow and heat transfer through a rectangular duct in the presence of a non-uniform transverse magnetic field, Journal of Magnetism and Magnetic Materials 31 (6) (2013) 31–42.

[39] A. Mohamad, J. Orfi, H. Alansary, Heat losses from parabolic trough solar collectors, International Journal of Energy Research 38 (2013) 20–28.

[40] E. Bellos, C. Tzivanidis, Thermal analysis of parabolic trough collector operating with mono and hybrid nanofluids, Sustainable Energy Technologies and Assessments 26 (2018) 105–115.

[41] A. Mwesigye, İbrahim Halil Yılmaz, J. P. Meyer, Numerical analysis of the thermal and thermodynamic performance of a parabolic trough solar collector using swcnts-therminol®vp-1 nanofluid, Renewable Energy 119 (2018) 844–862.